Extreme ultraviolet metalens by vacuum guiding

Marcus Ossiander[1]*†, Maryna Leonidivna Meretska[1]†, Hana Kristin Hampel[2]†, Soon Wei Daniel Lim[1], Nico Knefz[2], Thomas Jauk[2], Federico Capasso[1]*, Martin Schultze[2]*

Extreme ultraviolet (EUV) radiation is a key technology for material science, attosecond metrology, and lithography. Here, we experimentally demonstrate metasurfaces as a superior way to focus EUV light. These devices exploit the fact that holes in a silicon membrane have a considerably larger refractive index than the surrounding material and efficiently vacuum-guide light with a wavelength of ~50 nanometers. This allows the transmission phase at the nanoscale to be controlled by the hole diameter. We fabricated an EUV metalens with a 10-millimeter focal length that supports numerical apertures of up to 0.05 and used it to focus ultrashort EUV light bursts generated by high-harmonic generation down to a 0.7-micrometer waist. Our approach introduces the vast light-shaping possibilities provided by dielectric metasurfaces to a spectral regime that lacks materials for transmissive optics.

Dielectric metasurfaces consist of transparent nanostructures with subwavelength separation, which manipulate the phase of light on the nanoscale (*1*). This elaborate control is revolutionizing modern optics: Metasurfaces can replace bulk optics by thin and flat elements (*2*, *3*), combine multiple functions in single optical elements (*4*, *5*), and be used to realize innovative optical components that induce, for example, freely designable optical angular momentum (*6*) and polarization (*7*, *8*). Technology, including modern semiconductor lithography, demands this design liberty for innovative optical elements for ever-shorter wavelength radiation, but this development has been stalled at ultraviolet frequencies where dielectrics stop being transparent. To our knowledge, linear metaoptics have only been demonstrated down to a wavelength of ≈250 nm (*9*–*11*). Nonlinear metasurfaces reach further into the ultraviolet spectrum at the cost of indirect light-shaping mechanisms and have, at present, been demonstrated down to a wavelength of 185 nm (*12*–*15*).

Inaccessible to metasurface design has been extreme ultraviolet radiation (EUV), which covers the wavelength range from 10 to 121 nm and corresponds to a photon energy of 10 to 124 eV (*16*). This wavelength regime receives appreciable attention as a gateway to achieving attosecond temporal resolution in ultrafast spectroscopy (*17*) and lithographically fabricating nanometer-scale transistors in state-of-the-art semiconductor industry (*18*). However, today, all fields that use EUV radiation are encumbered by handling problems that arise from being limited to reflective or binary optics [e.g., toroidal mirrors or Fresnel zone plates; see (*19*) for an overview of existing technology]. Here, we present a new physical mechanism for metasurface design and demonstrate how linear metasurfaces can be realized at a wavelength of 50 nm, thus providing the foundation for general-purpose transmissive optics technology for EUV radiation.

[1]John A. Paulson School of Engineering and Applied Sciences, Harvard University, Cambridge, MA 02138, USA. [2]Institute of Experimental Physics, Graz University of Technology, 8010 Graz, Austria.
***Corresponding author. Email: mossiander@g.harvard.edu (M.O.); capasso@seas.harvard.edu (F.C.); schultze@tugraz.at (M.S.)**
†These authors contributed equally to this work.

Principle of vacuum guiding and metalens design

In the EUV, the strong absorption of most materials and their near-unity real part of the refractive indexes (*20*) usually prevent effective refraction or waveguiding. The refractive indexes of most dielectrics in the visible spectrum are determined by electronic transitions in the ultraviolet, that is, by resonances whose frequencies are higher than the frequency ω of visible light. In the Drude-Lorentz oscillator model, this results in a complex refractive index $\tilde{n}(\omega) = n(\omega) + i\kappa(\omega)$ for visible light, with a real part $n \geq 1$, the imaginary unit i, and a negligible absorption coefficient κ. By contrast, EUV light oscillates faster than these electronic resonance frequencies, resulting in $n \leq 1$ and a large absorption coefficient κ, which renders conventional transmissive metaoptics design unfeasible. For the same reason, EUV manipulation must rely on reflective glancing-angle mirrors in vacuum. The concept for metasurface design introduced here is visualized in Fig. 1: In the EUV spectrum, vacuum or air ($n = 1$) has a refractive index that is larger than that of a pillar made from $n < 1$ material; therefore, the pillar cannot guide or confine light. However, a void or hole ($n = 1$), that is, the absence of material, in a layer with material index $n < 1$ can act as a waveguide core surrounded by a lower-index cladding. Therefore, truncated waveguide metasurfaces are possible in the EUV by following an inverted design scheme that tunes nanohole dimensions instead of the shapes of free-standing nanostructures.

Materials with $n < 1$ that can be used to alize such metasurfaces exist throughout the EUV; for example, aluminum, silicon, and beryllium allow optics for the wavelength range from 40 to 90 nm; scandium and boron cover 20 to 40 nm; and rhenium, molybdenum, and zirconium cover 10 to 20 nm. Figure S1 compiles the refractive indexes and the transmission of these materials. Because of the availability of high-brightness laser-driven tin plasma sources, 13.5 nm is a wavelength of major importance for semiconductor lithography (*18*). At this wavelength, for example, ruthenium has the complex refractive index $\tilde{n} = 0.88 + 0.02i$ (*21*).

For the implementation of this concept, we chose a thin membrane of crystalline silicon as the base material and a cylindrical hole as the polarization-independent guiding structure. These are schematically shown (Fig. 1, A and C) together with the real part of the silicon refractive index in the EUV (*22*) and the transmission through a 220-nm-thick silicon layer (Fig. 1B). To highlight the vacuum-guiding behavior of the holes, the simulated intensity profile of light with a vacuum wavelength of λ_{vac} = 50 nm incident on such a perforated silicon membrane [80-nm hole diameter in a square 120-nm–by–120-nm unit cell, periodic boundary conditions; see section 1 of (*19*) for simulation details] is plotted in Fig. 1D: At the center of the membrane (110 nm after its front surface), 84% of the energy of an incident plane wave is transmitted within the hole, whereas 16% of its energy is transmitted in the silicon. However, the hole only covers 34% of the unit-cell area. Because most power is transmitted in vacuum, absorption in silicon is limited, and the overall transmission is enhanced relative to that of the unstructured film: An unstructured 220-nm-thick silicon membrane transmits 28% of incoming 50-nm light. Accounting for the 80-nm-diameter hole using its area coverage would increase transmission to 52%. Vacuum guiding increases the transmission further to 67%.

Although perforations have been used in nano-optics before, the presented guiding mechanism is fundamentally different from antiguiding in holes (*23*), low-index guiding in air (*24*), or hollow-core fibers (*25*). Furthermore, the enhancement does not require a periodic structure, which distinguishes the effect from extraordinary optical transmission (*26*).

To realize our EUV metasurface (Fig. 1A), with full design flexibility to emulate the phase profile of a desired optical element, we numerically created a library of meta-atoms based on the transmission phase of holes with 20- to 80-nm diameters in a 220-nm-thick silicon membrane [see section 1 of (*19*) for simulation details]. Notably, between wavelengths of 50 and 62 nm, the photon energy–dependent transmission phase is widely tunable by the

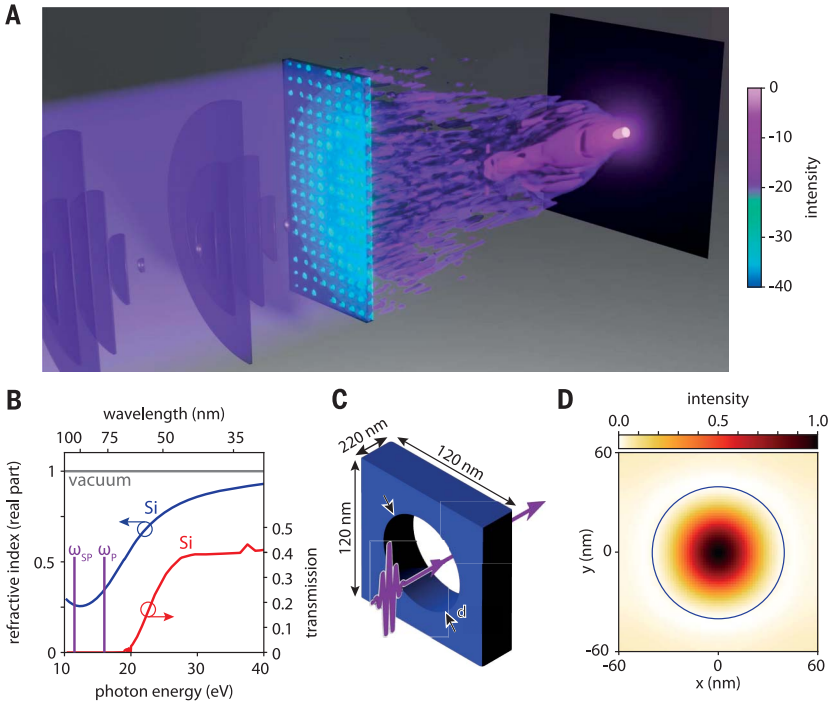

Fig. 1. Vacuum-guiding enables EUV metalenses. (**A**) Concept and simulation of a metalens that is focusing EUV: We impart the phase profile of an aspheric focusing lens on light pulses with a vacuum wavelength of 50 nm (purple disks) using holes through a silicon membrane (rectangular area). Because the refractive index of silicon is smaller than unity in parts of the EUV spectrum, holes through silicon concentrate incoming light. This effect relaxes subwavelength requirements for creating metasurfaces, allows us to impart a hole size dependent phase shift using feature sizes on the order of the vacuum wavelength, and increases transmission through the absorbing membrane. The false color plot illustrates this light concentration in the holes and how the ultraviolet radiation collapses into a focus after propagating the focal length. For better visibility, we cut the displayed metasurface and the light intensity distribution along a plane that includes the optical axis. Further simulation details are presented in Fig. 4. (**B**) Photon energy dependent real part of the refractive index of crystalline silicon [blue line, data from (*22*)] in the EUV spectrum and intensity transmission of a 220 nm thick silicon membrane (red line). The frequencies of the bulk ω_P and surface plasmon ω_{SP} are marked in purple. (**C**) Schematic and setup for meta atom simulation: EUV light (purple arrow) passes through a 220 nm thick crystalline silicon membrane (blue) with a hole with diameter *d*. We model a single unit cell (120 nm by 120 nm) with periodic boundary conditions. (**D**) Finite difference time domain simulation of EUV vacuum guiding through an 80 nm diameter hole in a 220 nm thick silicon membrane. The false color plot shows the transverse beam intensity profile of light with a vacuum wavelength of 50 nm at the midpoint of the silicon membrane along the propagation direction, that is, 110 nm after the front surface. The hole is indicated as a blue circle. The simulation setup in three dimensions is shown in (C). The hole covers 34% of the total area; however, 84% of the energy is transmitted within the hole and only 16% of the energy is found in silicon. The intensity decays exponentially into the silicon cladding because of the refractive index contrast. The overall transmission of the patterned 220 nm thick silicon membrane is 67%.

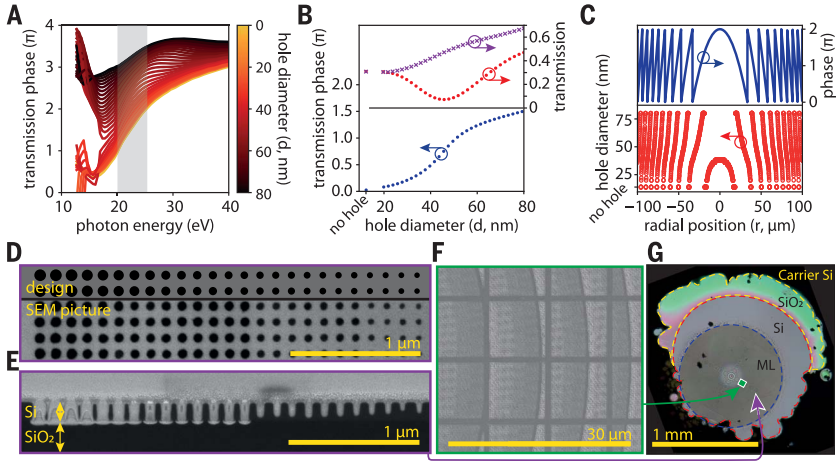

Fig. 2. Design and fabrication of an EUV metalens. (**A**) Photon energy dependent transmission phase of holes in a 220 nm thick silicon membrane (see Fig. 1C for the unit cell), color coded for different hole sizes. The gray area indicates the region where hole diameters from 20 to 80 nm offer phase coverage larger than 1.5π, which is enough to achieve efficient and diffraction limited focusing (*27*). (**B**) Overall hole diameter dependent intensity transmission (purple crosses) and transmission phase in the forward direction (blue circles) of the resulting meta atom library at 50 nm wavelength (25 eV photon energy). Because the 120 nm by 120 nm unit cell size is comparable to the wavelength, low diffraction orders can be generated for holes that cause a transmission phase shift close to π (diameters around 45 nm). When plotting only the transmission into the zeroth diffraction order (red circles) of a periodic array of same diameter holes, this causes a dip in the transmission. Because hole diameters spatially vary in a metalens and light from all holes interferes constructively to a focus, the more uniform overall transmission (purple crosses) is a better gauge to judge transmission uniformity. (**C**) Target transmission phase profile (blue line) of a metalens with focal length *f* = 10 mm at 50 nm wavelength, calculated from Eq. 1 modulo 2π, and the corresponding matched hole diameter (red circles) using the library of (B) to realize the metalens. (**D**) Shown at the bottom is a scanning electron microscope (SEM) picture of a 3 μm by 0.5 μm portion of the metalens with 1 mm diameter and 10 mm focal length designed for 50 nm wavelength. The position where the picture was taken on the metalens is marked by the purple arrow in (G). Shown at the top is the design of the metalens in this area [compare with (C)]. (**E**) Cross section of a metalens fabricated using the same recipe as the lens in (D) on the silicon on insulator carrier wafer obtained using focused ion beam milling and SEM. The position where the picture was taken on the metalens is marked by the purple arrow in (G). (**F**) Zoomed out SEM picture of a 34 μm by 31 μm portion of the metalens. The position where the picture was taken on the metalens is marked by the green rectangle in (G). The focusing pattern of the metalens is apparent from the ring segments, which show decreasing width from left to right. Every 10 μm, holes are omitted to increase the stability of the metalens, which is visible as a square scaffolding pattern. The symmetry of the scaffolding is intentionally different from the symmetry of the metasurface to increase stability. (**G**) Optical microscope picture of the final metalens membrane. The metalens (ML) is encircled by the dashed blue line. Because its features are too small to be resolved at this magnification, the metalens shows a moiré pattern (ring patterns and bright area at the center; an enlarged image is provided in fig. S4). The unpatterned silicon membrane area appears solid gray (encircled by the dashed red line). Areas with a remaining buried oxide layer appear red and green because of thin film interference (encircled by the dashed yellow line). The silicon carrier wafer appears black.

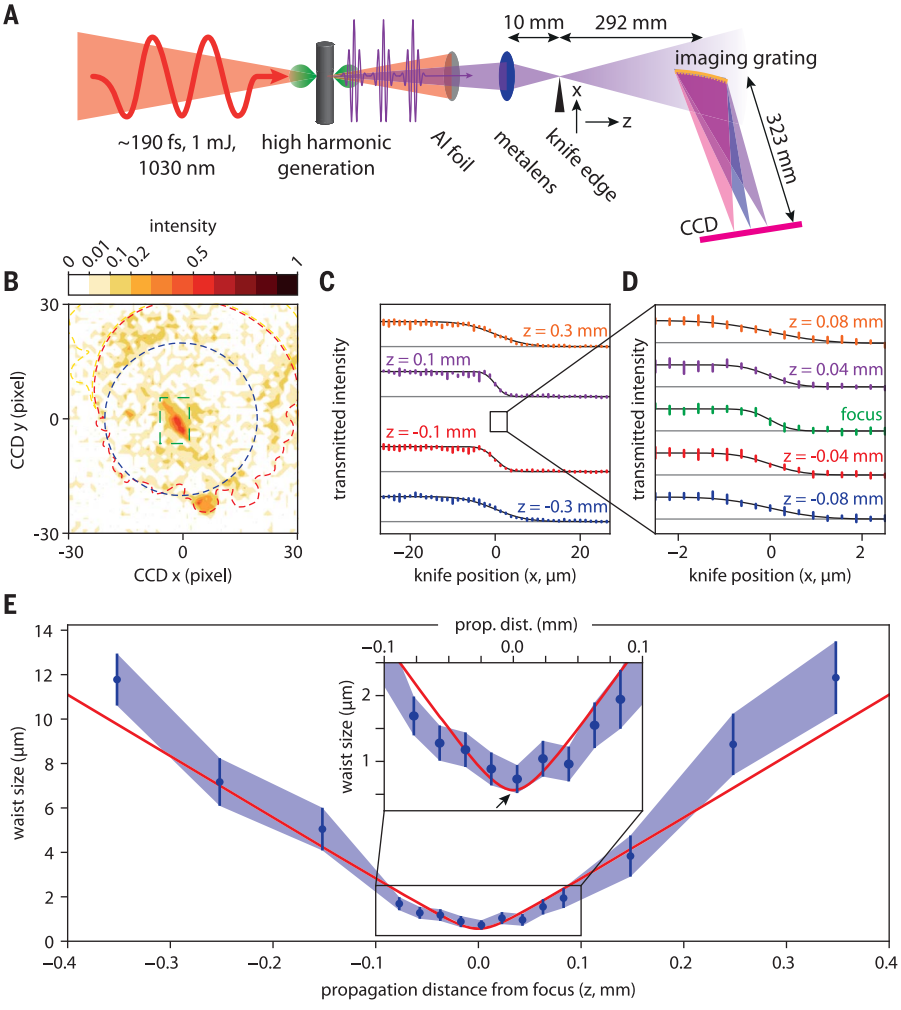

Fig. 3. Experimental demonstration of EUV metalens focusing. (**A**) An intense near infrared femtosecond laser pulse (red arrow and area) is focused into an argon gas target (green) to generate an attosecond pulse train (purple arrow and area) by high harmonic generation. Near infrared radiation is blocked using an aluminum filter foil (gray). The attosecond pulse train is then focused using the metalens (blue) pictured in Fig. 2. At the position of the focus along the propagation direction (marked *z*), a knife edge scan is performed using a razor blade mounted on a piezo stage moving along the transverse beam direction (marked *x*). Afterward, the attosecond pulse train's spectral components are split using a grazing incidence toroidal grating, and the focal plane is imaged on a charge coupled device (CCD) camera. (**B**) EUV beam profile after the metasurface (false color plot) at 25.3 eV photon energy (21st harmonic of the driving laser at 1030 nm wavelength) detected by the CCD. For comparison, we repeat the outlines from the microscopy image in Fig. 2G: The dashed blue line marks the metasurface, and the dashed red line marks the unpatterned silicon area. The granular structure with low intensity is already present in the incoming beam profile, which is plotted in fig. S5. The focal spot created by the metalens, which is imaged onto the CCD using the toroidal grating, is marked by the green dashed rectangle. It appears larger than the real focus because of the limited numerical aperture of the toroidal grating and aberrations caused by the imaging system. (**C**) Knife edge scans for different positions along the propagation direction of the metasurface focused beam [movement direction marked *z* in (A)]. The colored lines show the knife position dependent [movement direction marked *x* in (A)] integrated photon flux detected by the CCD camera in the focus area. As the razor blade moves into the focus, it blocks part of the transmitted radiation and decreases the transmitted flux. A large negative derivative of the flux represents a small focus. The error bars represent the standard deviation of three measurements. The black lines are least squares fits to the data assuming a Gaussian focus profile. (**D**) Same as (C) but in close proximity to the focus. The error bars represent the standard deviation of 10 measurements. (**E**) Propagation direction dependent waist sizes extracted from the fits in (C) and (D) (blue dots). The error bars represent the 95% confidence interval. The red line is a fit to the waist sizes assuming Gaussian beam propagation. The inset shows a zoomed in view of the propagation direction dependent waist size close to the focus [extracted only from the fits in (D)]. The minimum waist sizes reported in the text are marked by the black arrow.

hole diameter and offers more than 1.5π transmission phase coverage with an average transmission of 40% at 50 nm (see Fig. 2A for the photon energy–dependent transmission phase, Fig. 2B for the transmission and transmission phase at 50 nm, and fig. S2 for the photon energy dependent transmission). This transmission-phase coverage is enough to achieve efficient and diffraction-limited focusing, as explored, for example, in (*27*). The metasurface unit cell is shown in Fig. 1C, and the corresponding library is shown in Fig. 2B.

Experimental results

To experimentally prove that the vacuum-guiding concept yields viable EUV metalenses, we forward-designed a focusing EUV metasurface by mimicking the wavelength-dependent transverse hyperbolic phase profile (*28*)

$$\varphi(r,\lambda_{vac}) = -\frac{2\pi}{\lambda_{vac}}\left(\sqrt{r^2+f^2}-f\right) \qquad (1)$$

of an aspheric lens with focal length $f = 10$ mm in vacuum at transverse position $r = \sqrt{x^2+y^2}$ (x and y are the cartesian coordinates centered at the beam axis). This analog phase profile is matched by a simulated digital phase profile (sampled at positions x, y; $x = k\Delta x$; $y = l\Delta y$; $k, l \in \mathbb{Z}$; and $\Delta x = \Delta y = 120$ nm; k and l are integer indexes) using the hole library (Fig. 2B), yielding a recipe for the required hole-diameter distribution (Fig. 2C). The metalens is designed for a central vacuum wavelength of $\lambda_{vac} = 50$ nm, where silicon features a refractive index $\tilde{n} = 0.77 + 0.02i$. The smaller-than-unity real part at this wavelength partially relaxes the necessity for true subwavelength patterning, which facilitates the manufacturing of the meta-optical element. In the given implementation, the maximum feature size (80 nm) and unit cell size (120 nm) correspond to 1.2 and 1.8 times the inside-silicon wavelength λ_{Si}, respectively. Although this does not entirely prevent the formation of low diffraction orders that contain up to 53% of the transmitted light, it still allows the realization of numerical apertures up to NA $< \frac{\lambda_{vac}}{2\Delta x} = 0.2$ following the Nyquist theorem (*29*).

The demonstration sample, a free-standing metalens with a 1-mm diameter (numerical aperture $NA_{max} = 0.05$), is realized from silicon-on-insulator wafers [see section 2 of (*19*) and fig. S3 for fabrication details]. Figure 2, D and F, shows scanning-electron microscopy pictures of the final sample after metasurface etching but before membrane isolation. Figure 2G shows a light microscopy picture of the finished membrane, with thin-film interference colors confirming the complete removal of the buried oxide layer in the lens area. We achieved the designed hole diameters (see Fig. 2D) using both diameter-dependent electron beam lithography doses and diameter-dependent fabrication offsets [see section 2 of (*19*)]. A focused-ion-beam cut (Fig. 2E) through a sample reveals holes

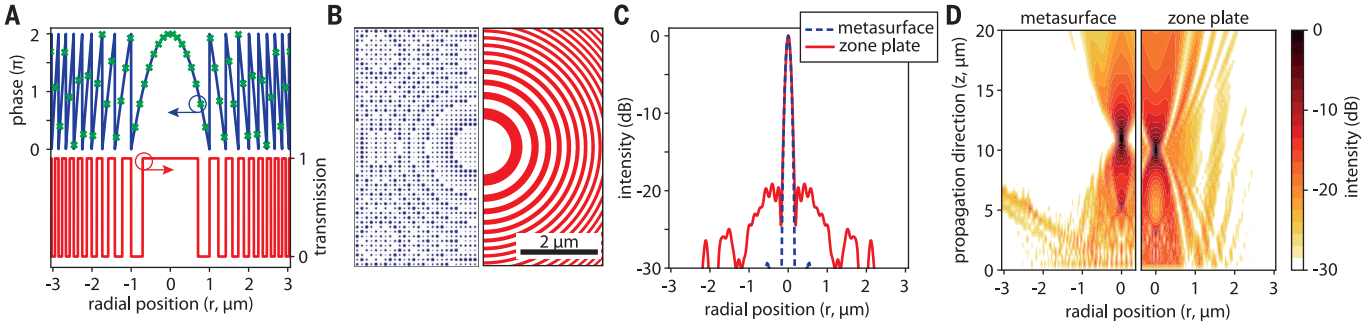

Fig. 4. Finite-difference time-domain modeling and benefits of an EUV metalens. (**A**) Target transverse phase profile (blue line) of a diffraction limited metalens (focusing length f = 10 μm, size 6 μm by 6 μm) designed for incoming light with 50 nm wavelength (25 eV photon energy) and sampling of this phase profile with the library presented in Fig. 2 (green crosses). As a comparison, the transmission profile of a binary intensity Fresnel zone plate with the same numerical aperture, focal length, and size is also shown (red line). (**B**) On the left is a two dimensional design of a metasurface that realizes the phase profile in (A). White areas represent a 220 nm thick silicon membrane, and blue areas represent holes through the silicon membrane. On the right is a two dimensional design of a binary intensity Fresnel zone plate that realizes the transmission profile in (A). White areas are perfectly transmitting, and red areas are perfectly absorbing. (**C**) Modeled transverse intensity cuts through the focus generated by the metasurface (blue dashed line) and the zone plate in (B) (red line) for incoming light with 50 nm wavelength (25 eV photon energy) and illumination by a Gaussian beam with a 2 μm waist. The zone plate focus has characteristic side lobes that are not present in the metasurface focus. (**D**) Shown on the left is the modeled light intensity evolution (false color plot) after the metasurface pictured in (B) focuses the Gaussian beam described in the caption of (C). Shown on the right is the modeled light intensity evolution (false color plot) after the zone plate pictured in (B) focuses the same Gaussian beam.

with square sidewalls and a partial etch of the smallest diameter holes. Because of the small transmission-phase difference between a membrane with small holes and a solid membrane (see Fig. 2B), the resulting phase error is smaller than 0.1π and can be corrected during meta-atom library calculation.

For experimental verification of the focusing power of the metalens, we generated diverging EUV attosecond pulse trains through near-infrared femtosecond laser pulse–driven high-harmonic generation in argon gas (*30*–*32*) [Fig. 3A and section 3 of (*19*)]. The frequency up-conversion extends up to the 35th order (42.1-eV photon energy, 29-nm wavelength) of the driving laser pulses (1.2-eV photon energy, 1030-nm wavelength), with spectral power concentrated around the laser's odd harmonics. A toroidal EUV grating disperses the spectral components of the attosecond pulse train and creates a frequency-resolved image of the focal plane on an EUV-sensitive camera where the metasurface's effect at the design wavelength can be inspected.

Figure 3B shows the beam profile at the focal plane of the metalens of the 21st harmonic with 25.3-eV photon energy and 49-nm wavelength (close to the design wavelength of the optics). The outline of the circular metasurface (dashed blue line) and features caused by the remaining silica aperture (dashed red and yellow lines; compare with Fig. 2G and fig. S4) are also visible. The bright focal spot at the metasurface center (dashed green line) presents experimental evidence for the viability of the EUV metalens to focus incident light.

Because the grazing incidence toroidal imaging grating provides a considerably smaller numerical aperture than the metasurface and introduces aberrations and astigmatism, the obtained image does not determine the focal spot diameter and underestimates the focusing power of the optical element. To determine the real focal spot size produced by the metasurface, we implemented a knife-edge scan [see Fig. 3A and (*33*)], where part of the focused beam in the focal plane is gradually blocked by a razor blade translated along the x direction indicated in Fig. 3A and the position-dependent transmitted intensity is recorded. As focusing concentrates the beam intensity along the transverse direction, the negative spatial derivative of the recorded x-dependent intensity reveals the beam profile. Figure 3, C and D, displays scan results for different planes along the propagation direction around the focus. Figure 3D includes a knife-edge scan that features a maximum negative spatial derivative, which is indicative of the focal plane. Under the assumption of a cylindrically symmetric Gaussian beam, the corresponding beam size is extracted by fitting an error function to the data at each position along the propagation direction (Fig. 3E) (*33*).

We observe that the metasurface focuses the illuminating beam to a minimum waist of $w_0^{\text{metasurface}} = 0.7 \pm 0.3$ μm [all reported waists w are measured using the $1/e^2$ intensity, that is, $I(r = \sqrt{x^2 + y^2} = w) = I(r = 0)/e^2$]. Using the Rayleigh-Sommerfeld diffraction integral (*34*), we calculated the minimum achievable waist $w_0^{\text{diffractionlimit}} = 0.45$ μm, assuming diffraction-limited focusing of our incoming beam (see fig. S5), which highlights that the metalens already performs within 1.6 times of the diffraction limit. For further comparison, the measured propagation distance–dependent waist size $w(z)$ can be fitted to that of a focused Gaussian beam with minimum waist w_0 (*35*) in vacuum:

$$w(z) = w_0\sqrt{1 + \left(\frac{z\lambda_{\text{vac}}}{\pi w_0^2}\right)^2} \qquad (2)$$

The fit (see Fig. 3E) suggests a minimum possible waist size of $w_0^{\text{metasurface}} = 0.56 \pm 0.03$ μm, which is even closer to the diffraction limit. Both results overlap within the experimental uncertainty. We attribute the deviation from the diffraction limit to imperfections in the EUV beam guiding and filtering optics and possible residual corrugations of the silicon membrane. For comparison, achieving similar spot sizes using the near-infrared driving laser would require close-to-unity numerical apertures; in the EUV, only a numerical aperture of 0.05 is required (*36*).

Aside from the focusing power, the transmission properties are crucial for future applications. Photons with wavelengths shorter than 100 nm possess enough energy to overcome the bandgap of all known dielectrics; therefore, large absorption is unavoidable (*37*). Nonetheless, owing to the vacuum guiding concept, our sample transmits more than 10% of all incoming 49-nm light and focuses 48% of the transmitted 49-nm light, which limits the root-mean-squared metalens wavefront error (*38*) due to fabrication accuracy to $\lambda_{\text{vac}}/10$ [λ_{vac} = 49 nm; see section 4 of (*19*) for details]. Such fine-granular phase control not only is a prerequisite for focusing but also opens the door for the future demonstration of optical angular

momentum plates and general holograms at EUV wavelengths.

Simulation of Nyquist-limited focusing

To further explore the potential of EUV metalenses, we investigated a metalens design with focal length f = 10 μm and overall optics diameter d = 6 μm (see Fig. 4A for the phase profile and Fig. 4B for the final design). We then simulated the focusing of a linearly polarized Gaussian beam using finite-difference time-domain modeling [illuminating Gaussian beam waist $w^{\text{illum.}}$ = 2 μm, and effective numerical aperture $\text{NA}_{\text{eff}} = \sin\left[\tan^{-1}\left(\frac{w^{\text{illum.}}}{f}\right)\right] \approx \frac{w^{\text{illum.}}}{f} = 0.2$ (*36*), which corresponds to the maximum realizable numerical aperture given by the Nyquist sampling theorem and our unit cell size (*29*); see section 1 of (*19*) for simulation details].

Figure 4D shows the formation of the metasurface focus. Even under these challenging conditions, the metasurface focus closely approaches the diffraction limit ($w_0^{\text{diffractionlimit}}$ = 85 nm) with a minimum beam waist $w_0^{\text{metasurface}}$ = 94 nm. The metalens focusing properties for a light pulse with extended bandwidth are explored in section 5 of (*19*) and fig. S6. Having the unit cell size be of the order of the design wavelength causes diffraction of ~53% of the incident power away from the beam axis into the diffraction orders of the quasi-periodic unit-cell arrangement. Adding an unpatterned layer of silicon with a refractive index n = 0.77 and a thickness on the order of half a wavelength after the metalens changes the grating condition in transmission and would prevent the creation of most of these propagating diffraction orders [because it limits the grating indices $p, q \in \mathbb{Z}$ that satisfy the transverse momentum wavevector condition $nk_0 = \sqrt{\left(\frac{2\pi p}{\Delta x}\right)^2 + \left(\frac{2\pi q}{\Delta y}\right)^2 + (nk_z)^2}$, with the overall momentum k_0 and the momentum along the layer normal k_z].

For thorough comparison, we also modeled the focal profile of a binary absorption zone plate with equal numerical aperture (see Fig. 4A for the absorption profile and Fig. 4B for the design). The juxtaposition of the focal profiles generated by the zone plate and the metalens shown in Fig. 4D highlights notable differences in focus quality and corroborates the benefit of the innovative metalens. A comparison with state-of-the-art technology [see (*39*) for a zone plate with comparable outermost zone width and section 6 of (*19*) for a summary of EUV focusing optics] highlights that the zone plate creates side lobes in its focal plane, which is an unavoidable property of zone plate foci (*40*). By contrast, because the metasurface realizes the focusing phase profile accurately by suppressing spherical aberrations, no sidelobes are visible. Furthermore, because vacuum guiding decreases absorption and no energy is lost to sidelobes, the maximum intensity in the metasurface focus exceeds that of the zone plate by 9%. The transverse focal cuts in Fig. 4C highlight this behavior: Unwanted features present in the focal plane are suppressed by more than 10 dB for the metasurface compared with the zone plate.

Concluding remarks

The transfer of metasurface technology, with its associated superior design freedom to the EUV spectral region, provides a general route to manufacture transmissive optics in this frequency range. This capability should lead to applications such as microscopy with unprecedented spatial and temporal resolution, orbital angular momentum beams with ultrahigh frequency, and structured light that has direct access to core-level electronic transitions in atoms and molecules. EUV lithography has become the main enabling fabrication technology that allows us to keep up with Moore's law (*18*); conversely, metasurface-based optics can be fabricated with deep ultraviolet lithography in the same semiconductor foundries of mainstream complementary metal-oxide-semiconductor (CMOS) technology (*27*). This convergence of semiconductor-processing technology and optics will expand to the realization of metaoptics using EUV lithography, further shrinking feature sizes and increasing the complexity of nanostructure shapes. In turn, with metasurfaces operating in the EUV, they will enable a new generation of lithography optics.

REFERENCES AND NOTES

1. S. M. Kamali, E. Arbabi, A. Arbabi, A. Faraon, *Nanophotonics* **7**, 1041 1068 (2018).
2. N. Yu *et al*., *Science* **334**, 333 337 (2011).
3. M. Khorasaninejad *et al*., *Science* **352**, 1190 1194 (2016).
4. N. Mahmood *et al*., *Nanoscale* **10**, 18323 18330 (2018).
5. C. Spägele *et al*., *Nat. Commun.* **12**, 3787 (2021).
6. R. C. Devlin, A. Ambrosio, N. A. Rubin, J. P. B. Mueller, F. Capasso, *Science* **358**, 896 901 (2017).
7. N. A. Rubin *et al*., *Science* **365**, eaax1839 (2019).
8. Y. Intaravanne, X. Chen, *Nanophotonics* **9**, 1003 1014 (2020).
9. Y. Deng *et al*., *Adv. Mater.* **30**, e1802632 (2018).
10. K. Huang *et al*., *Laser Photonics Rev.* **13**, 1800289 (2019).
11. C. Zhang *et al*., *Light Sci. Appl.* **9**, 55 (2020).
12. H. Liu *et al*., *Nat. Phys.* **14**, 1006 1010 (2018).
13. A. Ahmadivand *et al*., *Nano Lett.* **19**, 605 611 (2019).
14. M. Semmlinger *et al*., *Nano Lett.* **19**, 8972 8978 (2019).
15. M. L. Tseng *et al*., *Sci. Adv.* **8**, eabn5644 (2022).
16. W. K. Tobiska, A. Nusinov, in *35th COSPAR Scientific Assembly* (Committee on Space Research, 2004), pp. 1 10.
17. F. Krausz, M. Ivanov, *Rev. Mod. Phys.* **81**, 163 234 (2009).
18. B. Turkot, S. Carson, A. Lio, in *2017 IEEE International Electron Devices Meeting (IEDM)* (IEEE, 2017), pp. 14.4.1 14.4.3.
19. Materials and methods are available as supplementary materials.
20. A. Thompson *et al*., "X ray data booklet" (LBNL/PUB 490 Rev. 3, Lawrence Berkeley National Laboratory, 2009).
21. D. L. Windt, *Comput. Phys.* **12**, 360 370 (1998).
22. E. D. Palik, G. Ghosh, Eds., *Handbook of Optical Constants of Solids* (Academic Press, 1998).
23. S. W. D. Lim, M. L. Meretska, F. Capasso, *Nano Lett.* **21**, 8642 8649 (2021).
24. M. Hentschel *et al*., *Light Sci. Appl.* **12**, 3 (2023).
25. C. M. Smith *et al*., *Nature* **424**, 657 659 (2003).
26. T. W. Ebbesen, H. J. Lezec, H. F. Ghaemi, T. Thio, P. A. Wolff, *Nature* **391**, 667 669 (1998).
27. J. S. Park *et al*., *Nano Lett.* **19**, 8673 8682 (2019).
28. W. T. Chen *et al*., *Nat. Nanotechnol.* **13**, 220 226 (2018).
29. S. M. Kamali, E. Arbabi, A. Arbabi, Y. Horie, A. Faraon, *Laser Photonics Rev.* **10**, 1002 1008 (2016).
30. P. B. Corkum, *Phys. Rev. Lett.* **71**, 1994 1997 (1993).
31. M. Lewenstein, P. Balcou, M. Y. Ivanov, A. L'Huillier, P. B. Corkum, *Phys. Rev. A* **49**, 2117 2132 (1994).
32. A. L'Huillier, K. J. Schafer, K. C. Kulander, *J. Phys. At. Mol. Opt. Phys.* **24**, 3315 3341 (1991).
33. A. H. Firester, M. E. Heller, P. Sheng, *Appl. Opt.* **16**, 1971 1974 (1977).
34. R. L. Lucke, "Rayleigh Sommerfeld diffraction vs Fresnel Kirchhoff, Fourier propagation, and Poisson's spot" (NRL/FR/7218 04 10,001, Naval Research Laboratory, 2004).
35. B. E. A. Saleh, M. C. Teich, *Fundamentals of Photonics* (Wiley, 2007).
36. H. S. Chon *et al*., *J. Opt. Soc. Am. A Opt. Image Sci. Vis.* **24**, 60 67 (2007).
37. M. Ossiander *et al*., *Nat. Commun.* **13**, 1620 (2022).
38. M. Rimmer, *Appl. Opt.* **9**, 533 537 (1970).
39. J. Zhu *et al*., *Chin. Phys. B* **29**, 047501 (2020).
40. G. W. Webb, I. V. Minin, O. V. Minin, *IEEE Antennas Propag. Mag.* **53**, 77 94 (2011).
41. M. Ossiander *et al*., figshare (2023); https://doi.org/10.6084/m9.figshare.22191457.

ACKNOWLEDGMENTS

Funding: This work was performed, in part, at the Center for Nanoscale Systems (CNS), a member of the National Nanotechnology Coordinated Infrastructure (NNCI), which is supported by the NSF under award no. ECCS 2025158. CNS is a part of Harvard University. The computations in this paper were run on the FASRC Cannon cluster supported by the FAS Division of Science Research Computing Group at Harvard University. M.O. acknowledges funding by the Alexander von Humboldt Foundation (Feodor Lynen Fellowship), the Austrian Science Fund (FWF, Start Grant Y1525), and the European Union (grant agreement 101076933 EUVORAM). The views and opinions expressed are, however, those of the author(s) only and do not necessarily reflect those of the European Union or the European Research Council Executive Agency. Neither the European Union nor the granting authority can be held responsible for them. S.W.D.L. is supported by A*STAR Singapore through the National Science Scholarship Scheme. F.C. acknowledges financial support from the Air Force Office of Scientific Research (AFOSR) under award number FA9550 21 1 0312. **Author contributions:** M.O. developed the project, designed the metalenses, and conducted the numerical modeling. M.L.M. fabricated the samples. M.L.M., S.W.D.L., and M.O. imaged the samples. H.K.H., M.O., N.K., T.J., and M.S. designed, conducted, and analyzed the experiment. M.O., M.S., and F.C. wrote the manuscript. All authors discussed the final version of the manuscript. **Competing interests:** M.O., M.L.M., S.W.D.L., and F.C. have filed a provisional patent application (US 63/385,066). The authors declare no other competing interests.